

Published in final edited form as:

*Comput Med Imaging Graph.* 2012 December ; 36(8): . doi:10.1016/j.compmedimag.2012.08.001.

## Computer-aided Analysis of Airway Trees in Micro-CT Scans of Ex-vivo Porcine Lung Tissue

Christian Bauer<sup>a,b,\*</sup>, Ryan Adam<sup>c,d</sup>, David A. Stoltz<sup>c,d</sup>, and Reinhard R. Beichel<sup>a,b,c</sup>

<sup>a</sup>Dept. of Electrical and Computer Engineering, The University of Iowa, Iowa City, IA 52242

<sup>b</sup>The Iowa Institute for Biomedical Imaging, The University of Iowa, Iowa City, IA 52242

<sup>c</sup>Dept. of Internal Medicine, University of Iowa Hospital and Clinics, Iowa City, IA 52242

<sup>d</sup>Dept. of Biomedical Engineering, The University of Iowa, Iowa City, IA 52242

### Abstract

We present a highly-automated approach to obtain detailed structural models of airway trees from ex-vivo porcine lung tissue imaged with a high resolution micro-CT scanner. Such information is an important prerequisite to systematically study models of lung disease that affect airway morphology. The method initially identifies all tubular airway-like structures in the lung. In a second processing step, these structures are grouped into a connected airway tree by utilizing prior knowledge about the airway trees branching pattern. The method was evaluated on 12 micro-CT scans from four tracheal lobes of piglets imaged at three different inflation levels. For this study, two control piglets and two cystic fibrosis piglets were used. For systematic validation of our approach, an airway nomenclature was developed for the pig airway tree. Out of more than 3500 airway tree segments assessed during evaluation, 88.45% were correctly identified by the method. No false positive airway branches were found. A detailed performance analysis for different airway tree hierarchy levels, lung inflation levels and piglets with/without cystic fibrosis is presented in the paper.

### Keywords

airway tree segmentation; micro-CT; cystic fibrosis; airway tree; nomenclature; pig

## 1. Introduction

A number of lung diseases affect airway morphology including asthma, chronic obstructive pulmonary disease, and cystic fibrosis (CF). CF is a genetic disorder that occurs secondary to mutations in the gene encoding the anion channel termed the cystic fibrosis transmembrane conductance regulator (CFTR). CF affects the whole organism, but people with CF suffer primarily from severe lung disease, limiting their life expectancy [1]. In order to study CF and its pathogenesis, a porcine model of CF has been developed [2, 3, 4]. Over time, the CF pig develops lung disease that recapitulates many of the characteristics observed in humans with CF [5, 6]. At birth, the CF pig trachea and main bronchi are

© 2012 Elsevier Ltd. All rights reserved.

\*Corresponding author. Tel.: +1 319 335 4597; fax: +1 319 335 6028. christian-bauer@uiowa.edu (Christian Bauer).

**Publisher's Disclaimer:** This is a PDF file of an unedited manuscript that has been accepted for publication. As a service to our customers we are providing this early version of the manuscript. The manuscript will undergo copyediting, typesetting, and review of the resulting proof before it is published in its final citable form. Please note that during the production process errors may be discovered which could affect the content, and all legal disclaimers that apply to the journal pertain.

markedly reduced in caliber [7]. So far, the extent and patterning of the airway size reduction in the newborn CF pig airway tree for branches distal from the trachea is unknown. Identification of the anatomical patterning and quantification of a possible airway size reduction in the newborn CF pig airway tree will improve understanding of this congenital airway abnormality and its effect on disease pathogenesis.

As a prerequisite for such a study, methods are required to obtain highly detailed structural models of the airway trees with accurate radius and wall thickness measurements for individual airways. Based on this information, airways of animals with and without CF can be compared. While traditional computer tomography (CT) scanners are not equipped with a resolving capacity great enough to discern much beyond the largest airways of the newborn pig lung, micro computed tomography (micro-CT), a miniaturized version of conventional CT, allows imaging of the airways in much greater detail. An example of such a piglet lung micro-CT scan is shown in Fig. 1(a).

Fig. 1(b) shows the result of a manual segmentation of some airway branches in this dataset. A human user traced the airways in a few slices of the dataset and an algorithm produced segmentations in slices in between using interpolation. It took about 3 hours of user interaction to segment the shown set of airways. Thus, manual segmentation of the whole airway tree would be too time consuming to be practically feasible and highly automated methods are required instead.

Related work on (highly) automated airway tree segmentation in micro-CT scans of animals is rare. In many cases, such methods are highly optimized for a specific application and/or imaging protocol. For example, Artaechevarria et al. [8] and Shi et al. [9] presented methods for segmentation of airways in in-vivo micro-CT scans of mice lungs. Yavarna [10] presented a method for airway segmentation in ex-vivo mice lungs, which is based on a classifier and requires a large set of segmented datasets for training.

In contrast, segmentation of airway trees in CT scans of humans is a well studied area with existing commercial software packages available. Due to the lack of suitable methods for airway segmentation of animals imaged with micro-CT, it is not surprising that researchers in this field try to utilize and/or adapt segmentation methods developed for human airway segmentation. However, because of the differences in imaging (e.g., noise, artifacts, etc.) and anatomical differences, such attempts are not always successful.

In a recent study, Lo et al. [11] evaluated 15 automated and semi-automated airway segmentation methods on human lung CT scans. Most airway tree segmentation methods are based on region growing or front propagation methods, which make assumptions about the radio-density of the airway lumen in CT scans. To avoid leakage, some of the methods constantly monitor local segmentation results and adjust parameters accordingly. One example for such an approach is the method presented by Tschirren et al. [12]. It showed a good ability to extract a large number of airway branches without major leakages [11]. The method, which is part of the commercial software system "Pulmonary Workstation 2" (PW2) by VIDA-Diagnostics Inc., Coralville, IA, is based on an automated region-growing algorithm with leakage prevention and has a variety of interactive editing tools to correct errors in the initial segmentation (i.e. to remove leakage areas or to identify missing airways), if needed. In the same study by Lo et al. [11], two fully-automated methods presented by Bauer et al. [13, 14] showed comparable performance.

A priori it is not clear which methods compared in the study by Lo et al. [11] are promising for segmenting airways in ex-vivo piglet lung tissue imaged with micro-CT. For example, a segmentation result of a micro-CT scan generated with PW2 is depicted in Fig. 1(c). In this case, a lot of manual editing would be needed to generate a suitable segmentation result.

In this paper, we present a highly automated approach for extraction of structural models of airway trees from ex-vivo lung tissue imaged with micro-CT scanners. The method builds on a framework originally developed for the segmentation and separation of portal and hepatic vein trees in contrast enhanced CT scans [15], which showed promising results in segmenting human airways in CT scans in a preliminary study [14]. Specifically, we propose adaptations to this framework to deal with the large size of micro-CT images by means of a two-step tree reconstruction approach and investigate the applicability of this framework by studying segmentation performance on scans of CF and non-CF piglets. The centerline description generated with our approach can be used as input for algorithms that perform inner and outer airway wall segmentation. Such methods have been published [16] and are available in commercial lung image analysis software (e.g., PW2). In addition, the presented method might also be suitable as a starting point for other studies of airway trees imaged with micro-CT.

## 2. Image Data

Micro-CT scanners allow imaging of the porcine lung with high resolution. However, their field of view (FOV) is too small to accommodate the whole newborn pig lung. Hence, we have developed a micro-CT based protocol to image the newborn pig tracheal lobe, which is the porcine equivalent of the human right upper lobe and of appropriate size for micro-CT.

All animal protocols were reviewed and approved by the University of Iowa Animal Care and Use Committee. Non-CF (*CFTR*<sup>+/+</sup>) and CF (*CFTR*<sup>-/-</sup>) newborn pigs were provided by Exemplar Genetics (Sioux Center, IA). The animals were euthanized (Euthasol; Vibrac, Fort Worth, TX) for examination within 12 hours of birth, after which the tracheal lobes were excised and cannulated. The cannula was attached to an air source with adjustable pressure which allows to mimic different inflation levels (breathing states) of the lung. To mitigate tissue dehydration, the tracheal lobe was surrounded by damp medical grade gauze. An image of the setup and the cannulated piglet tracheal lobe is shown in Fig. 2.

After a lung recruitment maneuver, each tracheal lobe was scanned at different airway pressures including 0, 5, and 20 *cmH*<sub>2</sub>O. A Siemens micro-CAT II scanner (Siemens, Pre-Clinical Solutions; Knoxville, TN) was used for the micro-CT imaging. Scanner settings were as follows: 80 *kVp*, 200  $\mu$ A 1.5 *s* exposure, and 720 projections over 220 degrees of rotation. Image were reconstructed with an isotropic voxel spacing of 0.028 *mm* resulting in a typical dataset size in the range of 1070 × 660 × 960 voxels after cropping the scan to contain only the lung lobe.

Examples of resulting scans of newborn pig tracheal lobes are shown in Fig. 3. The main structures of interest are described in Fig. 3(a) and Figs. 3(b)-(d) show scans of the same lobe at different inflation levels. Note the effect of the different inflation levels on the airways as well as the lung parenchyma's appearance.

## 3. Airway Tree Structure Extraction Method

An overview of our approach to obtain the structure of an airway tree in micro-CT datasets is shown in Fig. 4. First, large-scale airway-like structures are extracted from the dataset after downsampling to half the size of the dataset in each dimension (Fig. 4(b)). From the extracted large-scale airway-like structures and a manually specified root branch of the tree an initial airway tree is obtained (Fig. 4(c)). Second, small-scale airways are identified (Fig. 4(e)) in the full-resolution micro-CT scan inside the lung parenchyma (Fig. 4(d)). Finally, the combination of the initial airway tree and the small-scale airway-like structures results in the final airway tree structure (Fig. 4(f)). Compared to the tree reconstruction proposed in

[15], this two-step approach enables processing of large size micro-CT datasets by lowering memory requirements and considerably reduces computing time.

In the micro-CT scans, the lung parenchyma is surrounded by damp gauze (Fig. 4(a)) which may be locally misinterpreted as containing smallscale airway-like structures. To address this issue, a rough lung parenchyma mask is utilized. This mask is generated as follows. The micro-CT image  $I$  is thresholded using  $I(\mathbf{x}) > -970$  HU and  $I(\mathbf{x}) < 0$  HU followed by morphological opening and closing [17] using a spherical structuring element with radius 0.5 mm. An example of a such obtained mask is shown in Fig. 4(d).

Basically, the outlined approach for extraction of the piglet airway tree structure is based on two different methods:

- a. a method for extracting airway-like structures from the dataset within a specified scale (radius) range and
- b. a method for grouping tubular structures into a complete airway tree based on structural properties.

Both methods are utilized twice in our algorithm. Initially for the main branches of the airway tree, and a second time to expand the airway tree with small scale airways. Details for both methods are presented in Sections 3.1 and 3.2.

### 3.1. Extraction of Tubular Structures

In micro-CT images, airways appear as elongated tubular structures that are surrounded by brighter (high density) tissue. Basically tubular structures can be identified by means of multi-scale tube detection filters [18, 19]. For our application, we utilize the approach presented in [15]. The output of the tube filter is converted to a centerline-based description of individual tubular structures by using a height-ridge traversal procedure, similar as in [15, 20]. The details of the tube extraction approach are provided below.

For every given location  $\mathbf{x}$  of the input image  $I$  a scale-dependent tube-likeness measure  $T(\mathbf{x}, \sigma)$  is obtained at a scale  $\sigma$  by using the following approach. Let  $G_\sigma$  be the Gaussian function at scale  $\sigma$ , and  $\mathbf{B}(\mathbf{x}) = \sigma \nabla(G_\sigma \star I(\mathbf{x}))$  and  $H(\mathbf{x}) = \sigma^2 \nabla^2(G_\sigma \star I(\mathbf{x}))$  be the scale-space normalized first order derivative (gradient) and second order derivative (Hessian matrix). Based on the eigenvalues  $|e_1|, |e_2|, |e_3|$  with associated eigenvectors  $\mathbf{v}_1, \mathbf{v}_2$ , and  $\mathbf{v}_3$  of the Hessian matrix, points inside of structures surrounded by brighter (higher density) tissue are identified as candidate tube points by  $e_1 > 0$  and  $e_2 > 0$ . For all candidate points, an offset medialness function and a central medialness function, which both capture complementary information, are calculated and combined into the final tube-likeness value.

The offset medialness function samples points along a circle with radius  $r = \sigma$  in the tubes cross-sectional plane spanned by  $\mathbf{v}_1$  and  $\mathbf{v}_2$ , as illustrated in Fig. 5. At these locations, the surface of the tubular structures shows high gradients pointing directly away from the center of the tube. Boundariness samples  $b_i = |\mathbf{B}(\mathbf{x} + r\mathbf{v}_{\alpha_i})\mathbf{v}_{\alpha_i}|$  with  $\mathbf{v}_{\alpha_i} = \cos(\alpha_i)\mathbf{v}_1 + \sin(\alpha_i)\mathbf{v}_2$  and  $\alpha_i = (2\pi i)/N$  are obtained at  $N = 32$  potential surface locations, resulting in  $\{b_1, b_2, \dots, b_N\}$  and their mean  $\bar{b}(\mathbf{x}, r)$  and variance  $s^2(\mathbf{x}, r)$ . For tubular structures, the mean of these boundariness samples is high and the variance is low. Thus, the offset medialness value is obtained by:  $T_0(\mathbf{x}, \sigma) = \bar{b}(\mathbf{x}, \sigma)(1 - s^2(\mathbf{x}, \sigma)/\bar{b}(\mathbf{x}, \sigma)^2)$ . At the centers of tubular structures the gradient vanishes. Thus, the magnitude of the gradient  $|\mathbf{B}(\mathbf{x})|$  can be utilized as an adaptive threshold to suppress responses away from the centers of the tubular structures. The final single-scale tube-likeness measure  $T(\mathbf{x}, \sigma)$  is obtained as  $T(\mathbf{x}, \sigma) = \max\{T_0(\mathbf{x}, \sigma) - |\mathbf{B}(\mathbf{x})|, 0\}$ .

To obtain the multi-scale tube detection filter response  $T(\mathbf{x}) = \max_{\sigma_0, \sigma_1, \dots, \sigma_n} \{T(\mathbf{x}, \sigma)\}$ , the responses at given scales  $\{\sigma_0, \sigma_1, \dots, \sigma_n\}$  are computed and the maximum selected as the final response; the scale of the final response also gives a radius estimate ( $r = \sigma$ ) and a tangent-direction estimate  $\mathbf{t} = \mathbf{v}_3$  of the tubular structure.

Based on the multi-scale tube detection filter response image  $T$ , centerlinebased representations are extracted using a height-ridge traversal procedure with hysteresis thresholding. Starting from all local maxima in the filter response image above a given threshold  $T(\mathbf{x}) > t_{high}$ , the height-ridge traversal procedure is started. Given a start point  $\mathbf{x}_0$  with associated tangent direction  $\mathbf{t}_0$ , the height ridge is traversed in direction  $\mathbf{t}_0$  and  $-\mathbf{t}_0$ . Given a current point  $\mathbf{x}_i$  on the centerline the next point on the centerline  $\mathbf{x}_{i+1}$  is selected as the local neighbor with the highest tube-likeness value  $T(\mathbf{x})$  under the constraint that  $\mathbf{t}_i \cdot \overrightarrow{\mathbf{X}_i \mathbf{X}_{i+1}} \geq 0$ . The traversal direction  $\mathbf{t}_{i+1}$  for point  $\mathbf{x}_{i+1}$  is updated to  $\mathbf{t}_{i+1} = \mathbf{t}_{i+1} \text{sign}(\overrightarrow{\mathbf{X}_i \mathbf{X}_{i+1}} \cdot \mathbf{t}(\mathbf{X}_{i+1}))$ . The traversal is repeated until no further centerline point above a threshold  $t_{low}$  is found or the next centerline point was already traversed before. The thresholds were set to  $t_{high} = 50$  and  $t_{low} = 20$  for the large and small scale airways.

With the above described algorithm, centerline based representations are extracted, where each centerline  $l^i$  consists of an ordered set of points  $\{\mathbf{X}_0^i, \mathbf{X}_1^i, \dots, \mathbf{X}_m^i\}$  with a corresponding radius estimate  $r_n^i$  and tangent direction estimate  $\mathbf{t}_n^i$  for each centerline point  $\mathbf{X}_n^i$ . To remove spurious noise responses, tubular structures shorter than 10 centerline points are discarded. For all remaining tubular structures, the radius and tangent directions are re-estimated by averaging over the  $\pm 5$  neighbors along the centerline.

As outlined in the introduction, large-scale and small-scale airway-like structures are extracted separately. For the large-scale airway-like structures the set of scales is  $\{0.09, 0.12, 0.15, \dots, 0.42\}$  mm and for the small-scale airway-like structures  $\{0.05, 0.07, 0.09\}$  mm. Figs. 4(b) and (e) show extracted large-scale and small-scale airway-like structures, respectively. The airways are visualized using cylinder elements at every centerline point with corresponding radius and tangent direction.

### 3.2. Tree Reconstruction

Airway trees have certain branching patterns. Thus, comparable rules can be utilized to identify the tubular structures associated with an airway tree, and consequently to discard other unrelated tubular structures. The tree reconstruction algorithm works as follows. Given a currently known tree structure (initially the main root branch), all unconnected tubular structures are considered as potential branches of the currently known tree. For each of these candidate branches, a connection confidence  $c(\mathbf{X}_n^i, \mathbf{X}_m^j)$  is calculated, representing the likelihood that the tubular structure is connected to the currently known airway tree. The tubular structure with the highest connection confidence is added to the tree structure, and the procedure is repeated as long as new tubular structures are identified that show a minimum connection confidence:  $c(\mathbf{X}_n^i, \mathbf{X}_m^j) \geq c_{min}$ . Unconnected branches are merged as children of the current tree structure. Thus, the final tree structure is guaranteed to be free of loops.

For calculation of the connection confidence  $c(\mathbf{X}_n^i, \mathbf{X}_m^j)$ , structural properties regarding branching angle, tube radius, and connection distance are considered. Therefore, we define for every centerline  $l^i$  the average radius  $r^i$  and the proximal/distal direction  $d^i$  as  $+1$ , if the

direction is from the first centerline point to the last one or  $-1$  otherwise. Between every endpoint  $\mathbf{X}_m^j$  of every unconnected tubular structure and every centerline point  $\mathbf{X}_n^j$  of the currently known tree, we define a distance  $d = \max\left(0, \left|\overrightarrow{\mathbf{X}_n^i \mathbf{X}_m^j}\right| - r_n^i\right)$  and angle  $\alpha = \angle\left(\overrightarrow{\mathbf{X}_n^i \mathbf{X}_m^j}, d^i t_n^i\right)$ . In order to be a plausible connection, the following properties have to be fulfilled:

- The radius must not increase considerably; i.e.  $r^j \leq \gamma r_{min}$  with  $r_{min}$  being the smallest branch radius along the whole path from the root of the tree.
- The branching angle must not be too large, i.e.

$$\alpha \leq \alpha_{max} \text{ and } \angle\left(\overrightarrow{\mathbf{X}_n^j \mathbf{X}_m^j}, d^j t_m^j\right) \leq \alpha_{max}.$$

- The connection distance must not be too large, i.e.  $d \leq d_{max}$ .

Only connection candidates fulfilling these properties are considered and the connection confidence  $c\left(\mathbf{X}_n^i, \mathbf{X}_m^j\right) = \exp\left(-\alpha/2\rho^2\right)\left(1+d/r^i\right)$  is calculated, which represents a trade-off between distance and branching angle. Parameters were set to  $\rho = 0.5$ ,  $\alpha_{max} = \pi/2$ ,  $d_{max} = 1.5$  mm,  $\gamma_r = 1.3$  and  $c_{min} = 0.0025$  for the large and small scale airways.

In our application, the tree reconstruction method is applied twice. First, on large-scale tubular structures and with a manually specified root branch to obtain an initial airway tree reconstruction. Second, the initial airway tree is completed by including small-scale tubular structures. The tube detection filter applied on small scales may produce responses inside large-scale tubular structures. To avoid that these branches are represented twice in the final tree structure, centerline points of small-scale airways  $\mathbf{x}_s$  inside of the large-scale airway tree are removed if  $\|\mathbf{x}_s - \mathbf{x}_l\| < r_l$  for any centerline point  $\mathbf{x}_l$  of the large-scale airway tree. Results of the initial and the final airway tree reconstruction step are shown in Figs. (c) and (f)4, respectively.

## 4. Evaluation Methodology

Twelve different micro-CT scans of the tracheal lung lobes from 4 different piglets were utilized for evaluation. None of these scans were utilized during algorithm development and parameter adjustment. Two of the piglets were CF pigs and two of them were non-CF pigs. For each piglet lung lobe, all three scans at pressure levels 0, 5, and 20  $cmH_2O$  were utilized for analysis.

In our evaluation, we analyzed the structural correctness of the extracted airway tree on different branching levels specified by an airway labeling scheme for the porcine airway tree. An expert with experience in analyzing piglet micro-CT datasets identified false positive and false negative side branches, based on which performance statistics were derived.

### 4.1. Airway labeling nomenclature

An airway labeling nomenclature is imperative for quantitative assessment and comparison of complex tree structures. For the human airway tree (bipodal) established labeling schemes exist. Also, the larger airways of the porcine lung (monopodial [21, 22]) have known names [23]. However, no porcine airway labeling scheme exists, which would cover the level of detail (i.e., number of airway generations) depicted in our micro-CT scans. Thus, we introduce our own nomenclature, which is illustrated in Fig. 6.

The nomenclature is structured by two fundamental units: the airway tier and the airway segment. The “airway tier” in the monopodial airway tree (i.e., in pigs) is analogous to the “airway generation” in the bipodal airway tree (i.e. in humans). When there is a branch in the tier based labeling scheme, the larger of the two child branches remains at the same tier level as it was prior to the branching, and the smaller of the two child branches assumes a tier level of the parent branch plus 1. One exception to this rule is the trachea, which is the only airway having a tier level of 0. The airways that branch directly off the trachea have a tier level of 1. This set of airways includes the tracheal bronchus, the left main bronchus, and the right main bronchus. Another exception is the tracheal bronchus (tier 1) which gives way to two tier 2 airways. The airways that bifurcate directly off the tier 1 airways constitute the tier 2 airways. In the tracheal lobe there are two tier 2 airways: the cranial (Cr) and caudal (Ca) branches (Fig. 6(b)). The airways that branch directly off the tier 2 airways constitute tier 3 airways. The tier 3 branches do not have established names and they are referred to generically in the nomenclature by the order in which they appear. The first branch is named “B1”, and the second branch “B”, and the nth branch “Bn”.

An airway segment is defined as a portion of an airway branch that ranges from one branchpoint to the next. Each segment in the airway tree has a unique label, consisting of a series of letters, numbers and periods. The letters denote specific airway branches, the periods separate airway tier levels, and the numbers denote branch numbers and the segment of interest position along the branch in which it resides. As one reads a tracheal lobe airway label from left to right, one begins at the trachea (abbreviated as “T” in the label) and descends the airway tree, by way of the tracheal bronchus (abbreviated as “TB”) to the airway segment of interest by the most direct route possible. The branches passed through en route to that segment are noted sequentially in that segments label.

#### 4.2. Performance Analysis

A human observer with experience in analyzing micro-CT scans of piglet lungs followed systematically all branches in the datasets with a tier of 1 to 3 and identified all missing and false positive child branches. Based on the so obtained information, performance statistics were calculated.

To facilitate this evaluation procedure, voxel accurate segmentations of the airway branches delineating the airway lumen were obtained using a graph-cut based segmentations that utilizes the available centerline/radius information as a shape prior [15]. Branches with tier 2, tier 3 and higher tier numbers were segmented separately and the resulting binary segmentations combined into one labeled volume dataset. These labeled volume datasets can be utilized to visualize the different tier branches in different colors using a standard medical imaging viewer (3D Slicer, [www.slicer.org](http://www.slicer.org)). Fig. 7 shows an example of such a visualization in a single slice of the micro-CT dataset. These visualizations allowed the human user to follow the individual branches at the different tiers systematically and mark errors in the segmentation.

### 5. Results

Fig. 8 shows examples of the segmentation results. In these visualizations, the branch levels are highlighted using different colors. Missing child branches identified by the human observer are indicated as small red spheres. Note, that the micro-CT scanner is not capable of imaging the whole piglet tracheal lobe due to its limited FOV and parts are truncated. For the dataset shown in Fig. 8(a)-(c), only parts of the cranial and caudal branch were imaged. For the dataset shown in Fig. 8(d)-(f) as much of the caudal branch was imaged as the micro-CT scanner permitted. The example in Fig. 8(c) shows the segmentation result obtained with our method on the dataset depicted in Fig. 1(a).

Because the cranial branch was only imaged in 6 out of the 12 evaluation datasets, we present statistical performance evaluation results focusing only on the caudal branch and its child branches. In the following, we refer to the caudal branch as Ca instead of using its full name T.TB.Ca.

In all datasets, the caudal branch was correctly identified. Fig. 9 shows how often individual tier 3 caudal branches were found/visible in the datasets. Fig. 10 summarizes how many tier 4 branches of the individual tier 3 branches were found/visible. A more detailed analysis of tier 4 branch detection and visibility rates can be found in Table 1. The plot shown in Fig. 11(a) compares the number of visible tier 4 branches between CF and non-CF piglets in dependence of parent branches. Fig. 11(b) depicts a similar plot for the percentage of found branches.

The human observer did not find any false positive child branches in the set of analyzed tier 3 and 4 branches. 98.04 % of all tier 3 branches were correctly found by the algorithm. On average, 145.25 tier 4 branches were visible out of which 84.76 % were identified by the algorithm. Specifically, at the different inflation levels of 0, 5, and 20  $cmH_2O$ , on average 98.25, 134.00 and 135.25 tier 4 branches were visible out of which 77.61 %, 83.88 % and 89.72 % were identified, respectively. Comparing datasets of piglets with and without cystic fibrosis, on average 135.50 and 151.00 tier 4 branches were visible out of which 90.01 % and 82.69 % were identified, respectively. Summarizing, out of the approximately 3500 airway segments that were investigated during the evaluation at the different tiers, 88.43 % were correctly identified by the algorithm.

## 6. Discussion

As can be seen from the segmentations shown in Fig. 8, in the monopodial branching pattern of the porcine airway tree, each branch continues at a bifurcation and tapers towards the end of the branch. Also, side branches decrease in caliber the more distal they are. Because airways become more difficult to detect in micro-CT scans the smaller they are—due to partial voluming and noise—this branching pattern has implications on the visibility and detection rate of side branches as analyzed in our evaluation. Towards the end of the continuously tapering branch, side branches' become harder to identify by humans and by automated algorithms. This pattern can be observed independent of the branch's tier number. As can be seen in Fig. 10 and Table 1, for more proximal side branches of an airway, many side branches were visible. On the other hand, for very distal side branches of the same airway, only few side branches were visible in the scans. And for all airways— independent of the number of visible side branches—towards the end of the branch some side branches were not identified by the algorithm.

Besides the limited resolution of the micro-CT scanner, two other factors have to be considered why certain branches might not be visible in the scans: (a) The branch does not physically exist in the lung tissue, or (b) the branch was outside of the FOV of the micro-CT scanner. The utilized micro-CT scanner had a limited FOV and was not able to accommodate the whole tracheal lung lobe, which makes the evaluation and comparison between CF and non-CF piglets more complicated. As can be seen in Fig. 8, only parts of the tracheal lobe were imaged. This also explains the behavior observed in Fig. 9. For half of the datasets, only the first part of the caudal branch was imaged in all 12 scans, while the more distal part of the caudal branch was only in the FOV in 6 of the datasets. However, even when the caudal branch was imaged completely, in none of the datasets more than 19 child branches of the caudal branch were observed in the scans.

In our evaluation, we considered micro-CT scans at different inflation levels from piglets with and without CF. With increasing inflation level, the lumen of the airways expands and thinner airways also become better contrasted. As a result, more airways were depictable in the scans with higher inflation level and our method was also able to identify a larger percentage correctly. Comparing scans from piglets with CF to piglets without CF, on average about 15 tier 4 branches fewer were visible, but the detection rate was about 7 % higher. Figs. 11(a) and (b) provide more details. When considering the number of visible tier 4 branches in dependence of parent branches (Fig. 11(a)), the similar trend can be observed for CF and non-CF piglets. Fewer tier 4 branches are visible for more distal tier 3 branches. Similar to the plot depicted in Fig. 10, fluctuations around the main trend can be observed, which can be explained by the different FOVs for the individual scans. Fig. 11(b) shows detection rates of tier 4 branches in dependence of tier 3 branches; no major differences can be observed between CF and non-CF piglet datasets.

Summarizing the overall performance of our method, 100 % of all tier 1 and 2 branches, 98.04 % of all caudal tier 3 and 84.76 % of tier 4 branches were identified by the algorithm. Moreover, the human observer did not find any false positive child branches in the set of evaluated branches down to a tier level of 3. As can be seen from Figs. 8(a)-(f) the method allows extraction of branches with even higher tier numbers. However, their structural correctness was not assessed.

The method is highly automated, and requires only the identification of a start branch. This process is simple, takes only a few seconds, and can be performed during the initial inspection of the micro-CT image data. Also, selecting a start branch allows the user to selectively analyze sub-trees, if needed.

The computation time of the algorithm was approximately 1.5 h per dataset, and the average size of micro-CT scans was  $1070 \times 660 \times 960$  voxels, after cropping datasets to the bounding box of lung tissue.

The proposed method was optimized for and evaluated on excised lung tissue of piglets. However, the method should also be applicable with adapted parameters (e.g. expected range of airway sizes) to excised lung tissue of other animals such as mice and rats imaged with micro-CT scanners.

The presented work facilitates research of lung disease. First, the substantially automated nature of our airway tree segmentation algorithm makes airway structure information more accessible. This is especially pertinent considering that alternate methods, notably manual segmentation, are commonly too labor intensive to serve as long term, practical solutions. Second, the method provides a relatively exhaustive description of the airway tree; it successfully obtains structural information even for distal airways with high tier numbers. This is particularly helpful for qualitatively studying airway pathologies. Third, extracting a structural airway model for micro-CT airway scans is a prerequisite of quantitative assessment of those airways.

Meyerholz et al. [7] used conventional CT imaging to study trachea and main bronchi size in neonatal CF pigs. In piglets with CF, the authors were able to show that these airways have a reduced caliber early in life, before the onset of inflammation and infection. However, with the used imaging and available image analysis methods, the authors were not able to study airway structure or size in more distal airways. Micro-CT imaging in combination with the proposed airway extraction method, the airway labeling nomenclature introduced in Section 4.1, and available quantitative measurement tools, will allow us to study the impact of CF on airways with an unprecedented level of detail. In addition, the presented work will facilitate

similar studies in humans, where the use of micro-CT has become increasingly common [24].

## 7. Conclusion

In this work, we presented a highly-automated approach to obtain detailed structural models of airway trees from ex-vivo porcine lung tissue imaged with high resolution micro-CT scanners. The method identifies all tubular airway-like structures in the lung tissue and groups them into a connected airway tree by utilizing prior knowledge about the airway trees branching pattern. In our evaluation on scans of piglets with and without CF imaged at different inflation levels, the method was able to extract 100 % of all tier 1 and 2 branches of the piglets, 98.04 % of all caudal side tier 3 and 84.76 % of tier 4 branches. No false positive branches were found. We believe, these methods will open up new avenues to systematically study lung disease in various research projects.

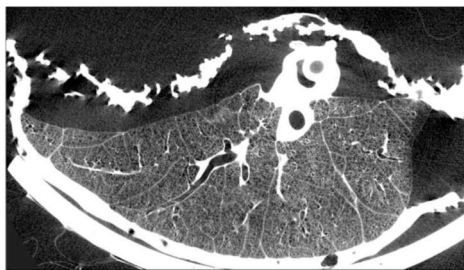
## Acknowledgments

The authors thank Teresa Ruggle for producing the airway tree nomenclature illustration. This work was supported in part by NIH grants HL111453, HL091842 and HL051670. David A. Stoltz is supported by the Gilead Sciences Research Scholars Program in Cystic Fibrosis.

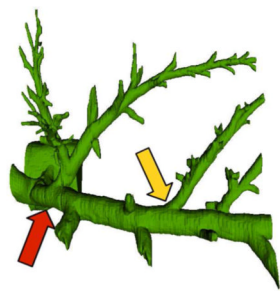
## References

1. Cystic Fibrosis Foundation. Cystic Fibrosis Foundation Patient Registry 2010 Annual Data Report. 2011. available from: <http://www.cff.org/UploadedFiles/LivingWithCF/CareCenterNetwork/PatientRegistry/2010-Patient-Registry-Report.pdf>
2. Rogers CS, Abraham WM, Brogden KA, Engelhardt JF, Fisher JT, McCray PB, McLennan G, Meyerholz DK, Namati E, Ostedgaard LS, Prather RS, Sabater JR, Stoltz DA, Zabner J, Welsh MJ. The porcine lung as a potential model for cystic fibrosis. *American Journal of Physiology - Lung Cellular and Molecular Physiology*. 2008; 295(2):L240–L263. [PubMed: 18487356]
3. Rogers CS, Stoltz DA, Meyerholz DK, Ostedgaard LS, Rokhlina T, Taft PJ, Rogan MP, Pezzulo AA, Karp PH, Itani OA, Kabel AC, Wohlford-Lenane CL, Davis GJ, Hanfland RA, Smith TL, Samuel M, Wax D, Murphy CN, Rieke A, Whitworth K, Uc A, Starner TD, Brogden KA, Shilyansky J, McCray PB, Zabner J, Prather RS, Welsh MJ. Disruption of the CFTR gene produces a model of cystic fibrosis in newborn pigs. *Science*. 2008; 321(5897):1837–1841. [PubMed: 18818360]
4. Rogers CS, Hao Y, Rokhlina T, Samuel M, Stoltz DA, Li Y, Petroff E, Vermeer DW, Kabel AC, Yan Z, Spate L, Wax D, Murphy CN, Rieke A, Whitworth K, Linville ML, Korte SW, Engelhardt JF, Welsh MJ, Prather RS. Production of CFTR-null and CFTR-DeltaF508 heterozygous pigs by adeno-associated virus-mediated gene targeting and somatic cell nuclear transfer. *The Journal of Clinical Investigation*. 2008; 118(4):1571–1577. [PubMed: 18324337]
5. Ostedgaard LS, Meyerholz DK, Chen J, Pezzulo AA, Karp PH, Rokhlina T, Ernst SE, Hanfland RA, Reznikov LR, Ludwig PS, Rogan MP, Davis GJ, Dohrn CL, Wohlford-Lenane C, Taft PJ, Rector MV, Hornick E, Nassar BS, Samuel M, Zhang Y, Richter SS, Uc A, Shilyansky J, Prather RS, McCray J, Paul B, Zabner J, Welsh MJ, Stoltz DA. The F508 mutation causes CFTR misprocessing and cystic fibrosis-like disease in pigs. *Science Translational Medicine*. 2011; 3(74):74–24.
6. Stoltz DA, Meyerholz DK, Pezzulo AA, Ramachandran S, Rogan MP, Davis GJ, Hanfland RA, Wohlford-Lenane C, Dohrn CL, Bartlett JA, Nelson T, George A, Chang EH, Taft PJ, Ludwig PS, Estin M, Hornick EE, Launspach JL, Samuel M, Rokhlina T, Karp PH, Ostedgaard LS, Uc A, Starner TD, Horswill AR, Brogden KA, Prather RS, Richter SS, Shilyansky J, McCray J, Paul B, Zabner J, Welsh MJ. Cystic fibrosis pigs develop lung disease and exhibit defective bacterial eradication at birth. *Science Translational Medicine*. 2010; 2(29):29–31.
7. Meyerholz DK, Stoltz DA, Namati E, Ramachandran S, Pezzulo AA, Smith AR, Rector MV, Suter MJ, Kao S, McLennan G, Tearney GJ, Zabner J, McCray J, Paul B, Welsh MJ. Loss of cystic fibrosis transmembrane conductance regulator function produces abnormalities in tracheal

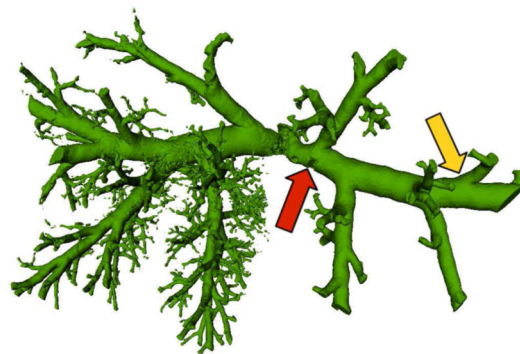
- development in neonatal pigs and young children. *American Journal of Respiratory and Critical Care Medicine*. 2010; 182(10):1251–1261. [PubMed: 20622026]
8. Artaechevarria X, Prez-Martn D, Ceresa M, de Biurrun G, Blanco D, Montuenga LM, van Ginneken B, Ortiz-de-Solorzano C, Muoz-Barrutia A. Airway segmentation and analysis for the study of mouse models of lung disease using micro-CT. *Physics in Medicine and Biology*. 2009; 54(22): 7009–7024. [PubMed: 19887716]
  9. Shi, L.; Thiesse, J.; McLennan, G.; Hoffman, EA.; Reinhardt, JM. Three-Dimensional Murine Airway Segmentation in Micro-CT Images. In: Pluim, JP.; Reinhardt, JM., editors. *Proc SPIE Conf Medical Imaging*. Vol. 6512. 2007.
  10. Yavarna, T. Master's thesis. University of Iowa; 2010. Airway segmentation of the ex-vivo mouse lung volume using voxel based classification.
  11. Lo P, van Ginneken B, Reinhardt JM, de Bruijne M. Extraction of airways from CT (EXACT'09). *International Workshop on Pulmonary Image Analysis, Vol 14 of Medical Image Computing and Computer Assisted Intervention*. 2010:175–189.
  12. Tschirren J, Yavarna T, Reinhardt JM. Airway segmentation framework for clinical environments, in: *International Workshop on Pulmonary Image Analysis. Medical Image Computing and Computer Assisted Intervention*. 2009:227–238.
  13. Bauer C, Bischof H, Beichel R. Segmentation of airways based on gradient vector flow, in: *International Workshop on Pulmonary Image Analysis. Medical Image Computing and Computer Assisted Intervention*. 2009:191–201.
  14. Bauer C, Pock T, Bischof H, Beichel R. Airway tree reconstruction based on tube detection, in: *International Workshop on Pulmonary Image Analysis. Medical Image Computing and Computer Assisted Intervention*. 2009:203–213.
  15. Bauer C, Pock T, Sorantin E, Bischof H, Beichel R. Segmentation of interwoven 3d tubular tree structures utilizing shape priors and graph cuts. *Medical Image Analysis*. 2010; 14:174–184.
  16. Liu X, Chen DZ, Wu X, Sonka M. Optimal graph search based image segmentation for objects with complex topologies. *Proceedings of SPIE*. 2009; 7258(1):725915–725915-10.
  17. Sonka M, Hlavac V, Boyle R. *Image Processing: Analysis and Machine Vision*. CL-Engineering (2nd). 1998
  18. Krissian K, Malandain G, Ayache N, Vaillant R, Troussset Y. Model-based detection of tubular structures in 3D images. *Computer Vision and Image Understanding*. 2000; 2(80):130–171.
  19. Pock T, Beichel R, Bischof H. A novel robust tube detection filter for 3d centerline extraction. *SCIA*. 2005:481–490.
  20. Aylward SR, Bullitt E. Initialization, noise, singularities and scale in height ridge traversal for tubular object centerline extraction. *IEEE Trans Med Imaging*. 2002; 21(2):61–75. [PubMed: 11929106]
  21. Wang PM, Kraman SS. Fractal branching pattern of the monopodial canine airway. *Journal of Applied Physiology*. 2004; 96(6):2194–2199. [PubMed: 15133015]
  22. Tajik JK, Tran BQ, Hoffman EA. Xenon-enhanced CT imaging of local pulmonary ventilation. *Proceedings of SPIE*. 1996; 2709(1):40–54.
  23. Nakakuki S. Bronchial tree, lobular division and blood vessels of the pig lung. *The Journal of Veterinary Medical Science/the Japanese Society of Veterinary Science*. 1994; 56(4):685–689. [PubMed: 7999892]
  24. McDonough JE, Yuan R, Suzuki M, Seyednejad N, Elliott WM, Sanchez PG, Wright AC, Geffer WB, Litzky L, Coxson HO, Par PD, Sin DD, Pierce RA, Woods JC, McWilliams AM, Mayo JR, Lam SC, Cooper JD, Hogg JC. Small-airway obstruction and emphysema in chronic obstructive pulmonary disease. *The New England Journal of Medicine*. 2011; 365(17):1567–1575. [PubMed: 22029978]



(a)



(b)



(c)

**Figure 1.** Micro-CT scan of an excised piglet lung lobe and airway tree segmentations. For orientation, corresponding locations are marked by arrows. (a) Cross-sectional image of the scan. (b) Typical complexity of a manual segmentation result, containing only a small subset of all airway branches. (c) Automated segmentation result produced with a commercial software system for airway segmentation in human lung CT scans (see text). Many airway branches remained unsegmented.

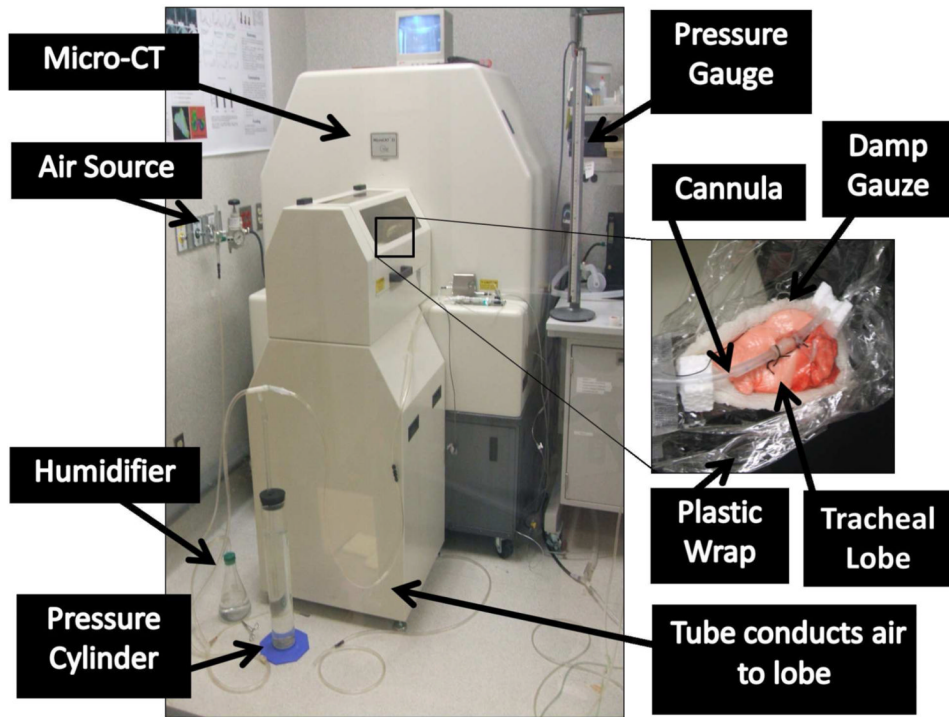


**Figure 2.**  
Micro-CT scanner with excised and cannulated tracheal lobe.

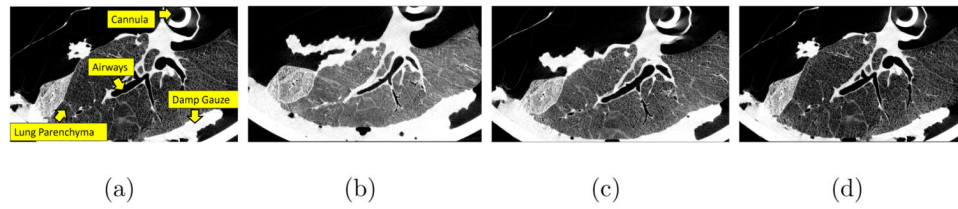


**Figure 3.** Cross-sections of obtained tracheal lobe micro-CT scans. (a) Labeling of structures of interest in the image data. (b)-(d) Micro-CT scans of the same piglet lobe at different inflation levels of (b) 0, (c) 5 and (d) 20  $cmH_2O$ . All datasets are shown with a gray-value windows of  $-930$  to  $70$  HU. Note that with increasing inflation level, the diameters of the airways change as well as the radio-density of parenchyma.

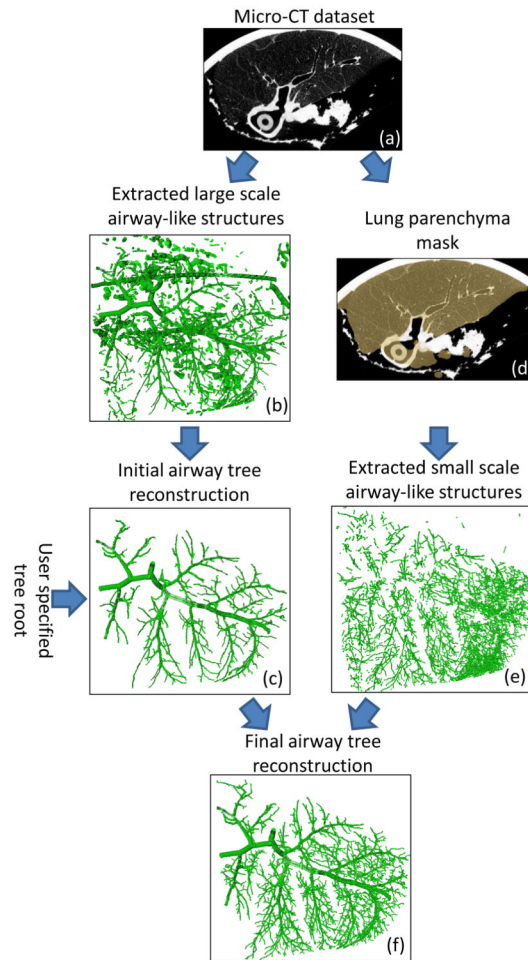


**Figure 4.** Method overview showing the processing steps.

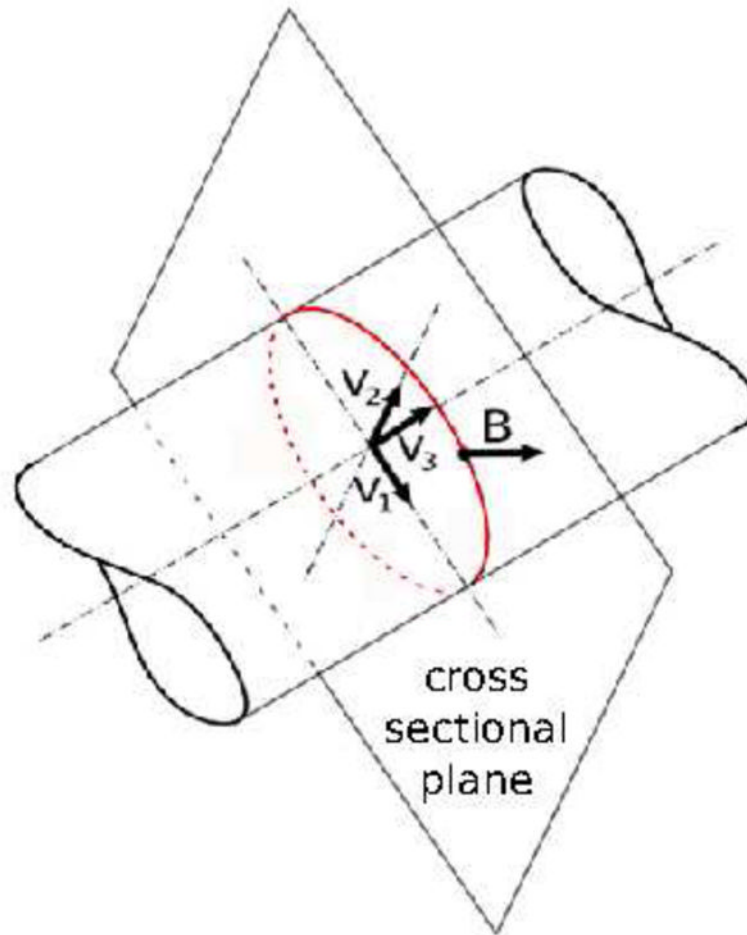


**Figure 5.** Offset medialness function calculation. Based on the eigenvector of the Hessian matrix, the tube's cross-sectional plane is estimated and boundariness samples are obtained at potential surface locations indicated by the the red circle.

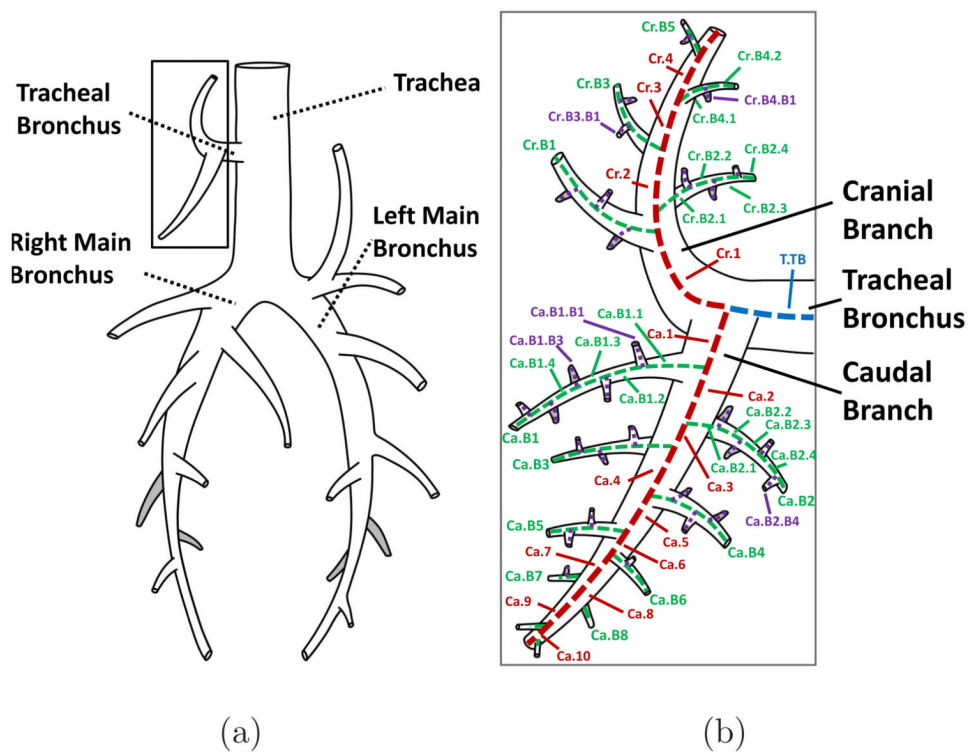


**Figure 6.** Pig airway tree nomenclature. (a) Larger branches. (b) Smaller branches in the tracheal lobe with their labels. All labels would begin with T.TB but this was omitted to save space. Branches with different tier numbers are shown in different colors: tier 1 (blue), tier 2 (red), tier 3 (green) and tier 4 (purple).

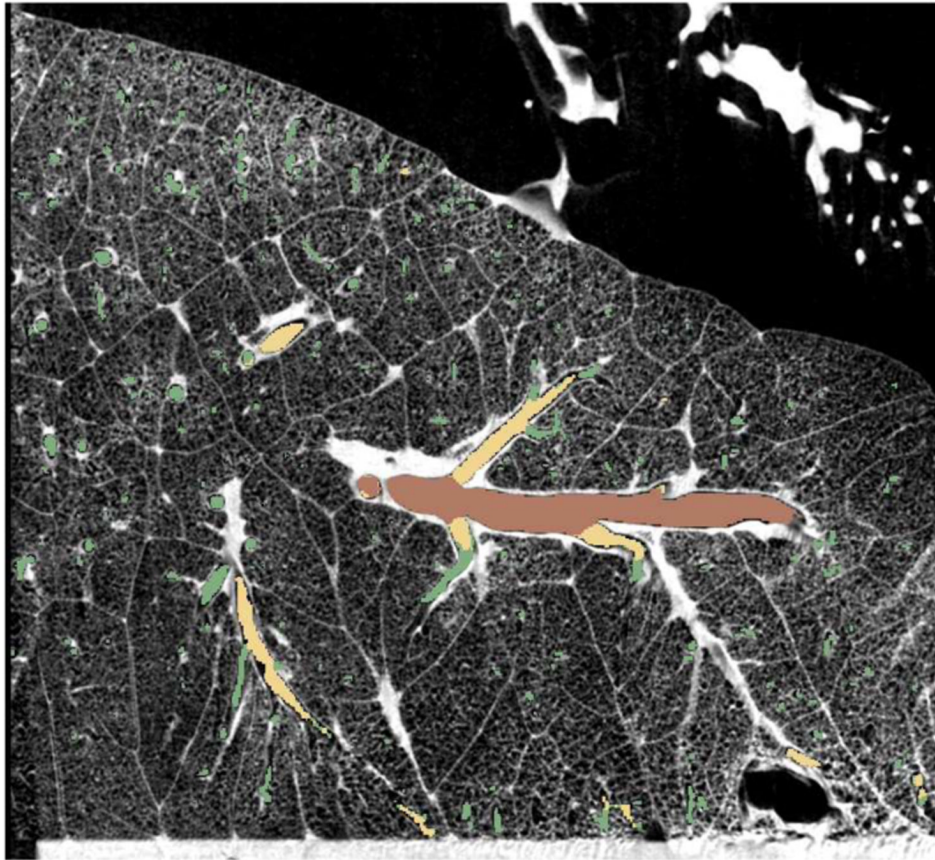


**Figure 7.** Micro-CT image showing overlaid airway segmentation results with different colors for different airway branch tiers. (brown) cranial/caudal tier 2 branches, (yellow) tier 3 branches, (green) tier 4+ branches.

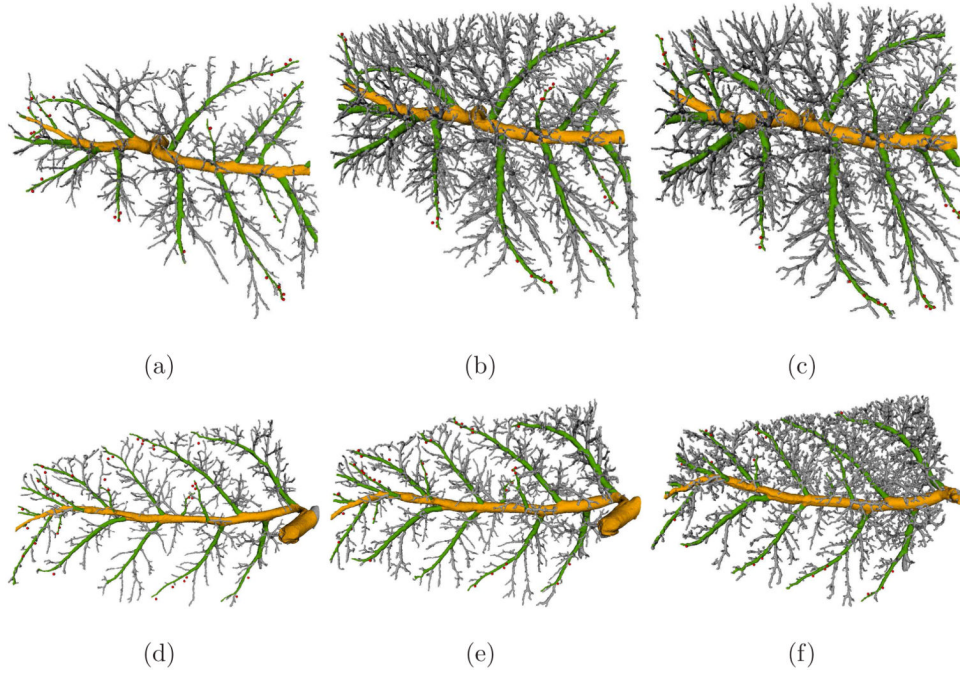


**Figure 8.** Airway segmentation results of two piglet micro-CT datasets imaged at different inflation levels of (a, d) 0, (b, e) 5 and (c, f) 20  $cmH_2O$ . (a)-(c) Dataset where parts of the cranial and caudal branch were imaged. For the dataset depicted in (d)-(f) only the cranial branch was imaged. Different airway branch hierarchy levels are shown in different colors: (yellow) cranial and caudal tier 2 branches, (green) tier 3 branches, (gray) tier 4+ branches. Identified missing child branches are indicated as small red spheres.

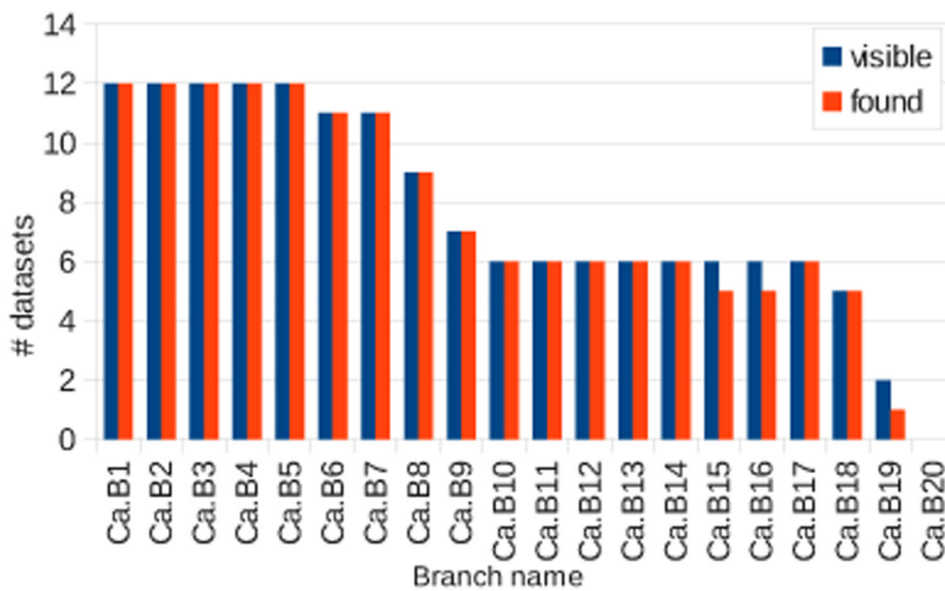


**Figure 9.** Statistics showing how often (in absolute numbers) individual tier 3 branches were visible/ found in the 12 evaluation datasets.

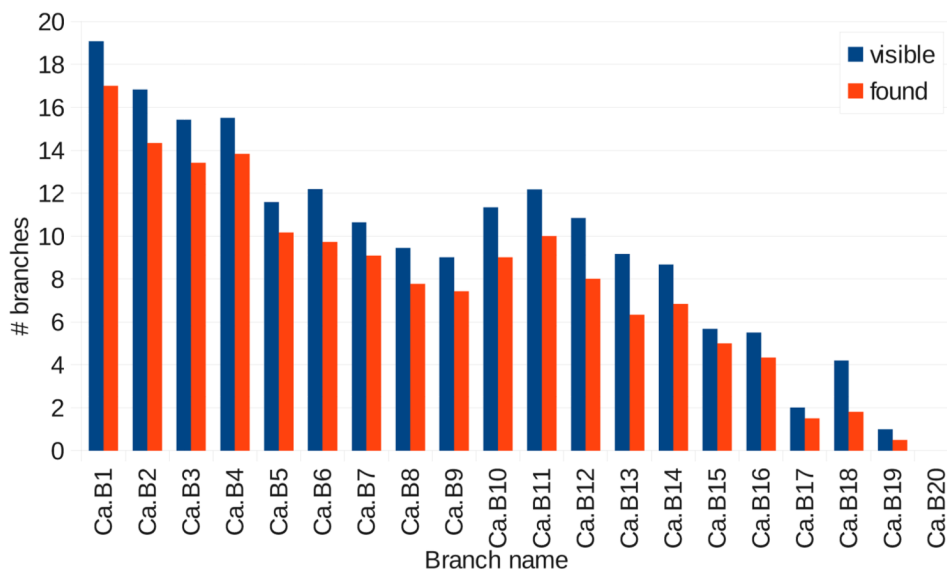
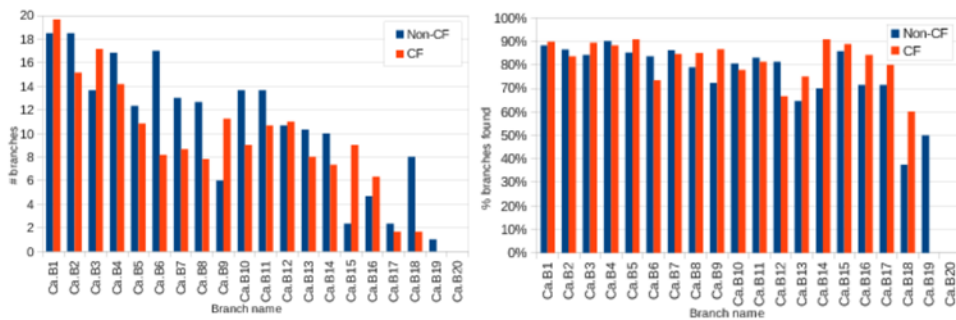


**Figure 10.** Average number of visible/found tier 4 branches depending on their tier 3 branch location, averaged over the number of scans where the tier 3 branch was actually visible.



(b)

**Figure 11.** Comparison between tier 4 branches of non-CF and CF piglets. (a) Average number of visible (manually identified) tier 4 branches in dependence of tier 3 branches. (b) Percentage of correctly identified tier 4 branches in dependence of tier 3 branches. In both cases, only visible branches were taken into account.

**Table 1**

Detailed statistics of detection rates and visibility rates for all tier 4 branches based on their location in the airway hierarchy as defined by the nomenclature. For example, for branch Ca.B8 the child branch #2 (Ca.B8.B2) was identified in 7 out of 8 cases where this branch was actually visible in the 12 evaluation datasets. An empty cell indicates that this branch was not visible in any of the evaluation datasets.

		Tier 4																									
		1	2	3	4	5	6	7	8	9	10	11	12	13	14	15	16	17	18	19	20	21	22	23	24	25	26
Tier 3 Caudal Branches	B1	12/12	12/12	12/12	12/12	12/12	12/12	12/12	12/12	12/12	12/12	11/12	11/12	11/11	10/11	8/11	6/11	5/10	6/8	4/6	3/5	3/4	2/2	2/2	0/2	1/1	1/1
	B2	12/12	12/12	12/12	12/12	12/12	12/12	11/12	8/12	12/12	8/12	11/12	9/11	8/11	8/9	6/9	6/7	3/6	3/4	1/2	2/2	1/2	0/2	1/2	1/2	1/1	
	B3	12/12	12/12	12/12	12/12	12/12	12/12	9/11	10/11	11/11	8/10	8/9	7/8	6/7	7/7	5/7	4/7	2/5	4/5	3/5	2/4	1/4	1/1	1/1			
	B4	12/12	12/12	12/12	12/12	12/12	12/12	11/11	11/11	11/11	10/11	6/11	9/11	10/11	8/11	8/10	6/10	3/4	1/2								
	B5	12/12	12/12	11/11	11/11	11/11	10/11	10/11	7/10	6/9	6/9	6/7	6/6	6/6	4/6	1/3	1/2	2/2									
	B6	11/11	11/11	11/11	11/11	8/11	9/11	5/11	6/9	7/8	5/8	4/7	4/6	4/5	3/3	1/3	2/3	3/3	1/1	1/1							
	B7	10/10	9/9	9/9	9/9	7/8	8/8	7/7	6/7	6/7	5/6	4/6	2/5	3/5	3/5	4/5	3/5	2/3	2/2								
	B8	7/8	7/8	8/8	7/7	7/7	5/7	5/6	5/5	3/5	5/5	2/4	2/4	1/3	2/3	2/2	2/2										
	B9	5/6	5/6	6/6	4/6	5/5	3/4	3/4	3/4	3/4	3/3	3/3	2/3	3/3	2/3	0/1	1/1										
	B10	6/6	6/6	6/6	5/6	6/6	4/5	4/5	2/4	3/4	2/3	2/3	3/3	2/3	1/3	2/2	0/1	0/1									
	B11	6/6	6/6	6/6	6/6	5/6	4/6	5/5	5/5	2/5	3/4	1/4	4/4	4/4	1/2	1/2	1/2										
	B12	6/6	6/6	5/6	6/6	4/6	5/6	5/6	2/5	2/5	3/4	1/3	1/3	2/2	0/1												
	B13	5/6	5/6	5/6	4/6	4/6	4/5	3/5	3/5	1/5	3/3	1/2															
	B14	5/6	5/6	6/6	5/6	5/6	6/6	3/6	3/4	1/3	1/2	1/1															
	B15	5/5	5/5	4/5	4/4	1/3	3/3	3/3	3/3	0/1	1/1	1/1															
	B16	5/5	4/5	4/5	2/3	2/3	1/2	1/2	2/2	1/1	1/1	1/1	1/1														
	B17	5/6	3/4	1/2																							
	B18	2/4	2/4	2/3	1/2	0/2	1/2	1/2	0/1	0/1																	
	B19	1/1	0/1																								
% found		95%	94%	96%	94%	88%	90%	82%	80%	77%	81%	73%	79%	85%	77%	69%	63%	59%	74%	67%	64%	60%	80%	25%	100%	100%	